Left ventricular geometry during unloading and the end-systolic pressure volume relationship: Measurement with a modified real-time MRI-based method in normal sheep.

Duc M. Giao[1,2,3], Yan Wang[4], Renan Rojas[1,2,3], Kiyoaki Takaba[1,2,3], Anusha Badathala[1,2,3], Kimberly A. Spaulding[1,2,3], Gilbert Soon[1,2,3], Yue Zhang[1,2,3], Vicky Y. Wang[1,2,3], Henrik Haraldsson[4], Jing Liu[4], David Saloner[1,4], Liang Ge[1,2,3], Julius M. Guccione[1,2,3], Arthur W. Wallace[1,2,6], and Mark B. Ratcliffe[1,2,3]

[1]Veterans Affairs Medical Center, San Francisco, California, USA, CA

Departments of Bioengineering[2], Surgery[3], Radiology[4] and Anesthesia[5], University of California San Francisco, San Francisco, CA, USA

Running Head: End-systolic Pressure Volume Relationship by Real-time MRI

Keywords: Left ventricle, Myocardial contractility, Pressure volume relationship, MRI, Left Ventricular Ellipticity

Text Word Count: 5572 words.

Corresponding Author: Mark B. Ratcliffe, MD, Surgical Services (112), Veterans Affairs Medical Center, 4150 Clement Street, San Francisco, California 94121. Telephone: (415) 221-4810. E-mail: Mark.Ratcliffe@va.gov

End-systolic Pressure Volume Relationship by Real-time MRI

Abstract

The left ventricular (LV) end-systolic (ES) pressure volume relationship (ESPVR) is the cornerstone of systolic LV function analysis. We describe a 2D real-time (RT) MRI-based method (RTPVR) with separate software tools for 1) semi-automatic level set segmentation (LSSM) of the LV, 2) generation of synchronized pressure area loops and 3) calculation of the ESPVR. We used the RTPVR method to measure ventricular geometry, ESPAR and ESPVR during vena cava occlusion (VCO) in normal sheep.

10 adult sheep were anesthetized and 2D cross sectional RTMRI performed at apex, mid-ventricle and base levels during separate VCOs. The Dice similarity coefficient was used to compare LSSM and manual image segmentation and thus determine LSSM accuracy. LV cross-sectional area, major and minor axis length, axis ratio, major axis orientation angle and ESPAR were measured at each LV level. ESPVR was calculated with a modified Simpson's rule method.

The Dice similarity coefficient between LSSM compared and manual segmentation by two readers was 87.31±2.51% and 88.13±3.43% respectively. All cross sections became more elliptical during VCO. The major axis orientation shifted during VCO but remained in the septo-lateral direction. LV chamber obliteration at the apical level occurred during VCO in 7 of 10 sheep. ESPAR was non-linear at all levels. Finally, ESPVR was non-linear because of apical collapse.

LSSM segmentation of 2D RT MRI images is accurate and allows calculation of LV geometry, ESPAR and ESPVR during VCO. In the future, RTPVR will facilitate determination of regional systolic material parameters underlying ESPVR.

2

End-systolic Pressure Volume Relationship by Real-time MRI

Word Count: 245 words

End-systolic Pressure Volume Relationship by Real-time MRI

Introduction

The left ventricular (LV) end-systolic pressure (ES) volume relationship (ESPVR) is the cornerstone of LV systolic function analysis [1, 2]. For instance, the slope of the ESPVR (end-systolic elastance (E_{ES})), which is usually measured during a transient reduction in preload (vena cava occlusion (VCO)) [3], is widely used in basic and clinical research as a load independent measure of global LV systolic function [4].

However, there are several gaps in our knowledge of ESPVR. First, at the myocyte level, it is generally accepted that the active force myocyte/sarcomere length relationship determines the ESPVR [5, 6] but little is known about how underlying systolic material properties relate to ESPVR. Second, LV systolic function is regionally heterogeneous in both the normal LV [7] and in patients with ischemic [8] and valvular heart disease [9, 10] but little is known about how regional systolic function contributes to the ESPVR. Imaging of the LV during VCO is a necessary prerequisite for investigation in both of these areas.

Conventional ESPVR methods including sonomicrometry [11] and the conductance catheter [12] provide limited LV geometry data. The 3D location of sonomicrometry transducers can be determined with the array localization method [13], however, the number of transducers is limited, wall thickness is usually measured at a single point [7] and calculation of LV geometry must assume an ideal LV shape [10]. Dahl et al measured both ESPVR with a conductance catheter and strain and strain rate with 2D echocardiography during VCO in normal pigs but LV geometry was not reported [14]. Segmental LV volume data can be obtained from a conductance catheter [15] but this provides only indirect information about segmental LV shape.

4

End-systolic Pressure Volume Relationship by Real-time MRI

Although conventional cine cardiac magnetic resonance imaging (CMRI) has excellent spatial resolution, acquisition times were not previously adequate for imaging during preload reduction. However, Zhang et al recently described a real-time CMRI (RTMRI) technique based on a radial FLASH sequence with nonlinear inverse reconstruction that has image acquisition times as short as 20 to 30 ms [16] and Witschey et al used the RTMRI method to acquire 2D images of the LV during VCO in normal sheep [17]. LV pressure area loops were created and the end-systolic pressure area relationship (ESPAR) was measured at a range of levels between the LV apex and base [18]. Nevertheless, the alterations in LV geometry during VCO have not been studied previously.

In the current study we describe a 2D RTMRI-based method (RTPVR) that includes separate software tools for 1) semi-automatic level set segmentation (LSSM) of the LV cavity, 2) generation of synchronized pressure area loops and 3) calculation of the ESPVR. We then use the method to measure ventricular geometry during VCO and corresponding ESPAR and ESPVR in normal sheep.

5

End-systolic Pressure Volume Relationship by Real-time MRI

Methods

Overview

Software tools for 1) semi-automatic level set segmentation (LSSM) of the LV (Matlab R2016b, Mathworks, Natick, MA, 2) generation of synchronized pressure area loops and 3) calculation of the ESPVR were created (C#, Visual Studio 2017, Microsoft, Redmond, WA with Matlab .net compiler). We first validated the LSSM method of LV cavity segmentation by comparing manual segmentation performed by two image readers with LSSM output. The Dice similarity coefficient, which determines the similarity of two image objects as the ratio of twice the object intersection over the union of the image objects, is commonly used to determine the accuracy of image segmentation methods [19]. Accordingly, intra- and inter-observer variabilities and the Dice coefficient were calculated to determine the accuracy of the LSSM method.

A flowchart illustrating the RTPVR method is shown in **Fig 1.** Briefly, separate 2D short axis RT MRI was performed at apex, mid-ventricle and base LV levels during separate VCOs. LSSM calculated LV short axis geometry was used to calculate major and minor axes, axis ratio and axis orientation. LV pressure and area are then synchronized and ESPAR loops are generated. Mixed model regression was used to determine the effect of LV level on major and minor axes, axis orientation and ESPAR slope and intercept. ESPVR is then calculated using a modified Simpson's rule method.

Fig 1. A flowchart illustrating the overall methodology designed to derive subject-specific ESPVR from RTMRI and LV pressure catheter measurement.

6

End-systolic Pressure Volume Relationship by Real-time MRI

Cardiac MRI (CMRI)

Studies were approved by the San Francisco VA Institutional Animal Care and Use Committee (IACUC), in compliance with the "Guide for the Care and Use of Laboratory Animals" prepared by the Institute of Laboratory Animal Resources, National Research Council.

Ten healthy, adult sheep were sedated with ketamine (20mg/kg intravenous), anesthetized (Isoflurane 2.2% inhaled) and mechanically ventilated. The tip of a pressure catheter (SPC-350; Millar, Houston, TX) was immersed in water at $38^{o}C$ for 12 hours prior to calibration and positioning in the LV and an 8 Fr balloon catheter was positioned in the inferior vena cava via femoral vessels using fluoroscopic guidance. Ferumoxytol (0.125 ml/kg IV over 1 hour; AMAG Pharmaceuticals, Waltham, MA) was given 1 hour prior to MRI [20]. Metoprolol (5 mg) and atropine (1 mg) were also given intravenously immediately prior to MRI. Isoflurane was maintained at 2.2%; end-tidal CO_2 was kept between 25 and 45 mm Hg; an infusion of neosynephrine was titrated to keep peak LV pressure at 90+5 mm Hg during cardiac MRI.

MRI imaging was performed on a 3T MRI scanner (Skyra; Seimens, Verlagen, Germany). Six cine long axis MR images that were 30° apart were first obtained and this set of baseline scans was used for LVV determination prior to VCO [21]. 2D short axis RTMRI was performed 25 (Apex), 50 (Mid) and 75% (Base) of the distance from the apex to the base of the LV during separate VCOs. The MR imaging parameters are summarized as follows: 2D multislice retrospectively-gated cine balanced steady-state free-precession acquisition with the following imaging parameters, TE = 1.34 ms, TR = 59.2 ms, acquisition matrix = 128 x 54, FOV = 178 x 260, slice thickness = 8 mm, pixel spacing = 2.0313 x 2.0313 mm.

7

End-systolic Pressure Volume Relationship by Real-time MRI

LV pressure (LVP) acquisition (12 bit, 5K samples/ sec, ACQ16 and Ponemah 5.2, DSI, St. Paul, MN) started approximately 5 seconds before the start of the MRI acquisition as shown in **Fig 2**. LV pressure was filtered with an in-line analog filter (BNC Low Pass Filter, Crystek, Fort Myers, FL) during acquisition and post-processed with a digital constrained least Pth-norm IIR filter (Matlab). LVP during VCO was calibrated using pressure acquired immediately prior to MRI acquisition as shown in **Fig 2B**.

Fig 2. Raw pressure data with noise prior to digital filtering and calibration (top) with the insert showing filtered and calibrated LV pressure during the selected VCO range.

Validation of semi-automatic level-set segmentation

Manual segmentation was used as the ground-truth to validate the accuracy of the level set algorithm [22, 23]. Manual segmentation was performed in a blinded manner. Two readers drew manual contours for 200 slices from all 10 subjects (20 slices for each case) as shown in **Fig 3A**. A second set of manual contours was drawn by each of the readers in 3 of the cases allowing the calculation of both inter- and intra-observer variability. The Dice similarity coefficient, commonly used to determine the accuracy of image segmentation methods, was used to determine the accuracy of the LSSM contours (**Fig 3B**) [19].

Fig 3. **(A)** Representative midventricular short-axis image of the LV showing level set and manual contours. Green = automatic contouring, Red = manual contour reader 1, Blue = manual contour reader 2. **(B)** Dice similarity coefficient for all 10 cases. (**C**) Representative midventricular short-axis image of the LV overlaid with automatic contours and fitted ellipse for quantifying major/minor axis length and major axis orientation angle as surrogate

8

End-systolic Pressure Volume Relationship by Real-time MRI

measurement of LV shape change. Red = fitted ellipse. Green = automatic contouring. Yellow circle = RV insertion point and centroid of ellipse.

Image segmentation

The LSSM was used to segment the 2D RTMRI images [24]. Specifically, the first frame of each imaging series was manually contoured while subsequent frames were processed with the LSSM [24].

LSSM generated contours were used to calculated LV cross-sectional area. In addition, an ellipse was fit to the LSSM generated contours and major and minor axes, axis ratio, and major axis orientation angle were calculated. Note that the orientation was relative to the anterior right ventricular endocardial insertion and the LV septum was in the positive direction **(Fig 3C)**.

Obliteration of the LV cavity was defined as LV area ≤ 0.25 cm^2. In instances where the LV cavity collapsed, axis and angle data were excluded. Representative LV shape and area changes during VCO are shown in **Fig 4.**

Fig 4. LV Area plot calculated by the level set algorithm with representative midventricular short-axis images of the LV before VCO and during VCO starting at t = 10 sec. Green makers = end-diastole (ED), Red markers = end-systole (ES).

ESPAR calculation

LV area was initially aligned to the region of noise on the unfiltered LVP trace. The time derivative of the LVP (d LVP/dt) was calculated and 0.25 peak d LVP/dt was aligned with peak LV area. The alignment method was chosen to obtain optimal LV PA loops (**S1 Figure**). The ESPAR was calculated using a shooting point iterative regression approach previously described by Kono et al for ESPVR determination from conductance catheter data [25].

9

End-systolic Pressure Volume Relationship by Real-time MRI

ESPVR calculation

LV volume at ES was determined with the following:

$$LVV(P)_{ES} = \sum_{i=1}^{5} \frac{1}{2} (LVA(P)_i + LVA_{i+1})(LVDist_{i+1} - LVDist_i) + LVV_{ES,0} \qquad (1)$$

where $LVA(P)_i$ is LV cross-sectional area with i ranges from 1 (LV apex) to 5 (LV valve plane), $LVDist_i$ is the distance of the real time MRI short-axis slices from the LV apex. Note that $LVDist_{5=ValvePlane}$ is assumed to move toward the apex in line with sonomicrometry data obtained in conscious dogs during VCO [26]. $LVV_{ES,0}$ is the baseline ES volume calculated from step 1 and is assumed to be constant during the VCO. Subsequent points on the ESPVR are generated using $LVA(P)_i$ at LVP range between 50 and 90 mmHg with a 5 mm Hg step change.

ESPAR and ESPVR calculation was performed with custom code written in C# (Visual Studio 2017, Microsoft, Redmond, WA) using Matlab routines (.NET assembly using Matlab Compiler, Mathworks).

Statistical analysis

All values are expressed as mean ± standard error of the mean. The significance level was set at $p<0.05$. Multivariate mixed effect analyses (Proc Mixed, SAS version 9.2, SAS Institute Inc., Cary, NC) were used to determine variable change during VCO. Individual sheep were included as a random effect [27]

10

End-systolic Pressure Volume Relationship by Real-time MRI

Results

Semi-automatic level set method

LSSM-based segmentation was automatic in 7 of 10 sheep data sets and required minor parameter modifications in the remaining 3 of 10 data sets. The intra-observer variability from the two readers were 0.54% and 0.88%. The Dice similarity coefficient was used for inter-observer variability measurement between level set segmentation comparing with manual results from two readers and determined to be 87.31%±2.51% and 88.13%±3.43% respectively, thus showing achieving a high segmentation accuracy as shown in **Fig 3B**. A representative LV area vs time plot is shown in **Fig 4**.

Hemodynamic parameters

Cycle length, ES interval and LV pressure at baseline are seen in **Table 1**. The ES interval was significantly shorter at the mid ventricle level (0.246+0.005 sec) than at the apical level (0.261+0.005 sec) but the cardiac cycle length was not different between LV levels. At baseline, the LVP was significantly lower at the apical level (88.6 $\pm$ 1.60 mm Hg) than both the mid-ventricle and basal levels (94.8 $\pm$ 1.34 and 95.1 $\pm$ 1.40 mm Hg respectively).

Changes in cycle length, ES interval and LV pressure during VCO are seen in **Table 2.** There was statistically significant shortening of both the ES interval (-0.0038+0.0005 sec/ beat) and cardiac cycle length (-0.0024+0.0004 sec/ beat) during VCO. For reference, this is a 4.8 msec decrease in cycle length over a 20 beat VCO. The rate of change of LVP during VCO was not different between LV levels.

11

Table 1. Baseline Cardiac MRI Measurements

	All VCOs (n=30)	Apex (n=10)	Mid (n=10)	Base (n=10)	Significance*
Cycle Length [sec]	0.637+0.007	0.631 + 0.008	0.640 + 0.012	0.641+ 0.014	NS
ES Interval [sec]	0.255+0.003	0.261 + 0.005	0.246 + 0.005	0.257 + 0.005	1, 3
LV Pressure at ES [mm Hg]	92.9+0.9	88.6 + 1.6	95.1 + 1.4	94.8 + 1.3	2, 3
LV Area at ES [cm^2]	5.43+0.25	2.53 + 0.156	4.55 + 0.181	9.15 + 0.323	1, 2, 3
LV Major Axis at ES [cm]	2.77+0.06	1.99 + 0.0601	2.637 + 0.0573	3.66 + 0.0627	1, 2, 3
LV Minor Axis at ES [cm]	2.37+0.06	1.63 + 0.0622	2.27 + 0.0456	3.20 + 0.0576	1, 2, 3
LV Axis Ratio at ES	1.19+0.01	1.26 + 0.0307	1.16 + 0.0150	1.15 + 0.0129	2, 3
Major Axis Orientation Angle at ES [^{o}]	31.7+3.7	13.7 + 7.46	51.2 + 5.67	29.9 + 4.74	1, 2, 3

Baseline cycle length, end-systolic (ES) interval, LV pressure and area, major and minor axis, axis ratio and axis angle at ES for all VCO data and at three LV levels. *NS: not significant, 1: Base vs Mid ($p<0.05$), 2: Base vs Apex ($p<0.05$), 3: Mid vs Apex ($p<0.05$).

Table 2. VCO Cardiac MRI Measurements

	All VCOs (n=30)	Apex (n=10)	Mid (n=10)	Base (n=10)	Significance*
Cycle Length [sec/ beat]	-0.0038+0.0005	-0.0027+0.0008	-0.0043+0.0011	-0.0042+0.0006	1
ES Interval [sec/ beat]	-0.0024+0.0004	-0.0035+0.0009	-0.0018+0.0008	-0.0020+0.0004	1
LV Pressure at ES [mm Hg/ beat]	-2.26+0.11	-2.32+0.19	-2.23+0.21	-2.22+0.18	1
LV Area at ES [cm^2/ beat]	-0.13+0.02	-0.08+0.02	-0.11+0.01	-0.21+0.04	1,2
LV Major Axis at ES [cm/ beat]	-0.038+0.003	-0.033+0.008	-0.040+0.004	-0.043+0.0058	1
LV Minor Axis at ES [cm/ beat]	-0.042+0.004	-0.033+0.009	-0.041+0.004	-0.050+0.008	1
LV Axis Ratio at ES	0.0080+0.0017	0.0084+0.0041	0.0072+0.0020	0.0085+0.0026	1
Major Axis Orientation Angle at ES [°/ beat]	-0.19+0.28	-1.04+0.46	-0.34+0.54	0.81+0.27	1,2

Slope of cycle length, end-systolic (ES) interval, LV pressure and area, and major and minor axis, axis ration and axis angle at ES vs VCO beat for all VCO data and at three LV levels. *1: All VCO variables vs beat ($p<0.05$), 2: Base vs Apex ($p<0.05$).

LV geometry

LV cross-sectional area, major and minor axes, axis ratio, and major axis orientation are shown in **Table 1**. As expected, LV area, major axis, and minor axis lengths increased from the apical to the basal segment. Conversely, axis ratios decreased from the apical to the basal segment, confirming that the LV is more spherical at the basal segment and more elliptical at the apical segment. Major axis orientation angle was greatest at the mid-ventricle level with an average angle of 51.2° while the base and apex levels had average angles of 29.9° and 13.7° respectively.

The change in LV cross-sectional area, major and minor axes, axis ratio, and major axis orientation during VCO are shown in **Table 2**. Also, **Fig 5** shows representative changes in major axis, minor axis, axis ratio, and major axis orientation angle at mid-ventricle LV level during VCO. Briefly, all 5 parameters changed significantly during VCO. The significant change in axis ratio documents that the LV becomes more elliptical during VCO and the significant change in major axis orientation shows that the major axis shifts during VCO but remains generally oriented in the septo-lateral direction.

There were statistically significant differences between LV levels in the rate of change of LV area (-0.08+0.02 cm^2/ beat apex vs -0.21+0.04 cm^2/ beat base level) and major axis orientation (-1.04+0.46 °/ beat apex vs 0.81+0.27 ° / beat base) during VCO. There was no difference in major and minor axis or axis ratio between LV levels during VCO.

Last, LV collapse at the apical segment during VCO was observed in 7 of the 10 cases (27 beats). **Fig 6** shows representative plots of LV area, major axis, and minor axis at the apical level. In each case, the dashed red line represents the time when LV cross sectional area fell

End-systolic Pressure Volume Relationship by Real-time MRI

below 0.25 cm^2.

Fig 5. Changes in LV geometry before and during VCO. Shape changes were quantified by 4 indicators calculated from the fitted ellipse: **(A)** Major Axis length, **(B)** Minor Axis length, **(C)** Major to Minor Axis Ratio, and **(D)** Major Axis Orientation Angle. Green makers = end-diastole (ED), Red markers = end-systole (ES).

Fig 6. Plots of LV Apical Area **(A)**, Major Axis length **(B)**, and Minor Axis length **(C)** of a case showing segmental collapse where LVA < 0.25 cm^2 after time = 15 sec as indicated by a red arrow.

ESPAR

Fig 7 shows representative LV pressure area loops during VCO at the apex, mid-ventricle and base levels. PA loops shift to the left and the slope of the ESPAR becomes more steep as the LV level moves from base to apex.

ESPAR slope and LV pressure intercept are illustrated in **Fig 8A, Fig 8B**, and **S1 Table**. The LV pressure intercept for the apex level was significantly higher than mid-ventricle (12.02 mm Hg) and base (8.39 mm Hg) levels mirroring the fact that the apical cavity obliterates before mid and base levels. The mixed-effect model showed that the ESPAR was non-linear (β_2= -0.500 (p<0.001), β_1=9.209 (p<0.001), β_0=48.73 (p<0.001)).

Fig 7. Representative LVP-area (LVPA) loops derived from the level set algorithm and pressure measurements along with fitted ESPAR at apex **(A)**, mid-ventricle **(B)**, and base **(C)** during VCO. The ESPAR was fitted with a linear function (blue) and a quadratic function (green) for comparison. The vertical dashed line represents collapse of the LV to zero volume.

15

End-systolic Pressure Volume Relationship by Real-time MRI

Fig 8. Slope of ESPAR (A) and LV area intercept A_o (B) at apex, mid, and base LV levels for all animals indexed to basal surface volume.

ESPVR

ESPVR, calculated using modified Simpson's rule (**Equation 1**), are shown in **Fig 9** and **S2 Table.** A representative ESPVR is shown in **Fig 9A.** Overall, we found E_{ES} to be extremely reproducible between animals (E_{ES} = 2.31$\pm$ 3.1 mm Hg/ml **(9B)**; V_o= -13.6$\pm$2.41 mL **(9C)**). The mixed-effect model showed that the ESPVR is nonlinear (β_2=0.0414 (p<0.001), β_1=0.349 (p<0.001), β_0=18.12 (p<0.001)).

Fig 9. Representative ESPVR with a quadratic fit in red dashed line **(A).** End-systolic elastance E_{ES} **(B)** and volume intercept V_o **(C)** of ESPVR indexed to basal surface volume.

16

End-systolic Pressure Volume Relationship by Real-time MRI

S1 Table. Slope and volume intercept of ESPAR

Animal #	ESPAR Slope [mm Hg/cm^2]			A_o [cm^2]		
	Apex	Mid	Base	Apex	Mid	Base
1	4.18	26.3	11.0	-18.5	-0.858	-1.63
2	11.6	23.4	9.07	-4.87	-0.543	-2.80
3	9.67	8.08	6.68	-4.52	-0.395	-2.28
4	18.0	16.6	8.13	-2.97	-0.820	-3.69
5	13.3	13.5	4.75	-3.63	-2.61	-12.5
6	9.28	7.80	6.84	-4.25	-4.04	-1.50
7	10.8	26.0	19.9	-5.29	-0.675	-1.07
8	8.67	13.1	7.86	-9.20	-4.03	-3.32
9	13.1	15.0	5.54	-4.55	-1.69	-7.75
10	8.51	14.1	10.4	-9.48	-2.30	-2.46
Mean + SEM	10.7 + 1.16	16.4 + 2.13	9.02 + 1.36	-6.73 + 1.48	-2.15 + 4.59	-3.90 + 1.12

End-systolic Pressure Volume Relationship by Real-time MRI

S2 Table. End-systolic elastance E_{ES} and volume-axis intercept

Animal #	E_{ES} [mm Hg/mL]	V_o [mL]
1	3.26	-8.21
2	1.87	-16.0
3	1.38	-18.4
4	2.35	-12.7
5	1.74	-29.2
6	1.57	-15.4
7	2.51	-11.2
8	1.96	-16.6
9	1.79	-6.64
10	4.70	-7.73
Mean + SEM	2.31+3.10	-13.6+2.41

18

Discussion

The principal finding of the study is that the RTPVR method allows measurement of LV geometry during VCO and calculation of corresponding ESPAR and ESPVR in normal sheep. Specific findings included that the LV shape becomes more elliptical during VCO leading to eventual apical LV cavity obliteration and that ESPAR and ESPVR are non-linear.

Semi-automatic active contouring

In the current study, an LSSM software tool was used to semi-automatically segment the LV during VCO. Briefly, semi-automatic LSSM generated contours were comparable to manual segmentation. The computation time for semi-automatic segmentation was less than 10 seconds per slice, although more powerful computing could greatly shorten the processing time.

LV geometry and apical level cavity obliteration during VCO

The effect of VCO on LV shape during ESPVR measurement has not been previously studied. However, similar to our findings, existing LV geometry data changes in a non-concentric fashion during VCO. For instance, Olsen et al. showed that the anterior posterior (AP) minor axis decreases more than the septal-lateral (SL) minor axis during VCO [28]. Furthermore, LV cavity obliteration occurs in the setting of intra-operative hypovolemia [29] and it is therefore seemed likely that LV cavity obliteration occurs during VCO.

The reason for the increased LV ellipticity during VCO where the major axis orientation is in the septo-lateral direction is unclear but could be due to either differential structural stiffness or transmural pressure in the interventricular septum. We did not measure right ventricular (RV) pressure. However, Olsen et al measured LV and RV pressure during VCO in conscious normal dogs and found that the ratio of LV to transmural septal pressure at ES is relatively constant

19

End-systolic Pressure Volume Relationship by Real-time MRI

(Calculated from Olsen Figure 5) [30]. Further work is warranted but this finding suggests that the septum may be structurally different than the LV free wall.

Contijoch et al. observed a similar increase in ESPAR pressure intercept at the LV apex in their real time MRI based study in normal sheep. However, that study did not observe cavity obliteration at the LV apex [31]. We used a neosynephrine infusion to counteract anesthesia related hypotension and maintain peak LV pressure at 90 mm Hg. As a consequence, LV pressure change during VCO in our study was somewhat higher. This may have been a factor and it is also possible that the volume status of sheep in the two studies was different.

ESPVR

Implicit in ESPVR analysis is the assumption that there is a relationship between the pressure volume relationship and regional systolic myocardial parameters [1]. Determination of that relationship would be complex and would probably require an inverse finite element (FE) solution where LV geometry and cavitary pressure are input and regional contractility is adjusted so that calculated myocardial deformation agrees with measured values [32]. However, such a FE based determination of the ESPVR/ regional contractility relationship would not be possible without imaging-based determination of LV geometry during VCO.

It is now generally accepted that the ESPVR is non-linear. For instance, van der Velde found that ESPVR is convex with center of curvature to the right and quadratic term (β_2) approximately -0.3 mm Hg/ ml^2 in normal pigs (Calculated for control values from van der Velde Table 2) [33]. We found that ESPAR at all LV levels is significantly non-linear. We also found that ESPVR is significantly non-linear with curvature to the right but with β_2 = -0.0414. Further study is warranted but non-linearity of ESPAR and the difference in β_2 between our

20

End-systolic Pressure Volume Relationship by Real-time MRI

study and van der Velde's suggests that ESPVR non-linearity is the product of both underlying material properties and apical cavity obliteration.

Limitations

With the current method we are able to acquire 6-8 images per beat which we interpolate to create PA loops. Further, synchronization between pressure and area is based on pressure and area metrics rather than the ECG.

Last, LSSM segmentation of the LV long axis during VCO was thought to not be possible because of algorithm failure to distinguish LV and left atrium at the mitral valve level.

Conclusions and future directions

In conclusion, LSSM segmentation of 2D RT MRI images is accurate and allows measurement of LV geometry during VCO and calculation of corresponding ESPAR and ESPVR. Although the goal was to describe the RTPVR method, it was noted that LV shape becomes more elliptical during VCO leading to eventual apical LV cavity obliteration and that ESPAR and ESPVR are non-linear.

Future work will focus on semi-automatic segmentation of the LV long axis during VCO with machine learning based methods. Hopefully, more rapid image acquisition as well as actual 3D RTPVR methods will also be developed. Last, similar RTPVR methods should be developed for the end-diastolic pressure volume relationship and, as before, the RTPVR will facilitate determination of the relationship between ESPVR and underlying regional systolic material parameters.

21

End-systolic Pressure Volume Relationship by Real-time MRI

Acknowledgements

22

References

1.   Burkhoff D, Mirsky I, Suga H. Assessment of systolic and diastolic ventricular properties via pressure-volume analysis: a guide for clinical, translational, and basic researchers. Am J Physiol Heart Circ Physiol. 2005;289(2):H501-12. Epub 2005/07/15. doi: 289/2/H501 [pii]

10.1152/ajpheart.00138.2005. PubMed PMID: 16014610.

2.   Suga H, Sagawa K. Instantaneous Pressure-Volume Relationships and Their Ratio in the Excised, Supported Canine Left Ventricle. Circulation Research. 1974;35(1):117-26. doi: 10.1161/01.res.35.1.117.

3.   Spratt JA, Tyson GS, Glower DD, Davis JW, Muhlbaier LH, Olsen CO, et al. The end-systolic pressure-volume relationship in conscious dogs. Circulation. 1987;75(6):1295-309. Epub 1987/06/01. PubMed PMID: 3568332.

4.   Sagawa K. The end-systolic pressure-volume relation of the ventricle: definition, modifications and clinical use. Circulation. 1981;63(6):1223-7. doi: 10.1161/01.cir.63.6.1223.

5.   Farman GP, Gore D, Allen E, Schoenfelt K, Irving TC, de Tombe PP. Myosin head orientation: a structural determinant for the Frank-Starling relationship. Am J Physiol Heart Circ Physiol. 2011;300(6):H2155-60. Epub 2011/04/05. doi: 10.1152/ajpheart.01221.2010. PubMed PMID: 21460195; PubMed Central PMCID: PMCPMC3119094.

6.   Gordon AM, Pollack GH. Effects of calcium on the sarcomere length-tension relation in rat cardiac muscle. Implications for the Frank-Starling mechanism. Circ Res. 1980;47(4):610-19. Epub 1980/10/01. PubMed PMID: 7408137.

7.   Biederman RW, Young AA, Doyle M, Devereux RB, Kortright E, Perry G, et al. Regional Heterogeneity in 3D Myocardial Shortening in Hypertensive Left Ventricular Hypertrophy: A Cardiovascular CMR Tagging Substudy to the Life Study. J Biomed Sci Eng. 2015;8(3):213-25. Epub 2016/03/25. doi: 10.4236/jbise.2015.83021. PubMed PMID: 27011783; PubMed Central PMCID: PMCPMC4800488.

8.   Kramer CM, Lima JA, Reichek N, Ferrari VA, Llaneras MR, Palmon LC, et al. Regional differences in function within noninfarcted myocardium during left ventricular remodeling. Circulation. 1993;88(3):1279-88. Epub 1993/09/01. PubMed PMID: 8353890.

9.   Knutsen AK, Ma N, Taggar AK, Brady BD, Cupps BP, Pasque MK. Heterogeneous distribution of left ventricular contractile injury in chronic aortic insufficiency. Ann Thorac Surg. 2012;93(4):1121-7. Epub 2012/03/03. doi: 10.1016/j.athoracsur.2011.12.067. PubMed PMID: 22381452; PubMed Central PMCID: PMCPMC3563333.

10.   Maniar HS, Brady BD, Lee U, Cupps BP, Kar J, Wallace KM, et al. Early left ventricular regional contractile impairment in chronic mitral regurgitation occurs in a consistent, heterogeneous pattern. J Thorac Cardiovasc Surg. 2014;148(4):1694-9. Epub 2014/09/28. doi: 10.1016/j.jtcvs.2014.05.088. PubMed PMID: 25260278; PubMed Central PMCID: PMCPMC4423555.

11.   Rankin JS, McHale PA, Arentzen CE, Ling D, Greenfield JC, Jr., Anderson RW. The three-dimensional dynamic geometry of the left ventricle in the conscious dog. Circ Res. 1976;39(3):304-13. Epub 1976/09/01. PubMed PMID: 782742.

12.	Baan J, Van der Velde E, De Bruin H, Smeenk G, Koops J, Van Dijk A, et al. Continuous measurement of left ventricular volume in animals and humans by conductance catheter. Circulation. 1984;70:812-23.

13.	Ratcliffe MB, Gupta KB, Streicher JT, Savage EB, Bogen DK, Edmunds LH, Jr. Use of sonomicrometry and multidimensional scaling to determine the three-dimensional coordinates of multiple cardiac locations: feasibility and initial implementation. IEEE Trans Biomed Eng. 1995;42(6):587-98. doi: 10.1109/10.387198. PubMed PMID: 7790015.

14.	Dahle GO, Stangeland L, Moen CA, Salminen PR, Haaverstad R, Matre K, et al. The influence of acute unloading on left ventricular strain and strain rate by speckle tracking echocardiography in a porcine model. Am J Physiol Heart Circ Physiol. 2016;310(10):H1330-9. Epub 2016/03/13. doi: 10.1152/ajpheart.00947.2015. PubMed PMID: 26968547; PubMed Central PMCID: PMCPMC4895836.

15.	Tulner S, Steendijk P, Klautz R, Bax J, Schalij M, Vanderwall E, et al. Surgical ventricular restoration in patients with ischemic dilated cardiomyopathy: Evaluation of systolic and diastolic ventricular function, wall stress, dyssynchrony, and mechanical efficiency by pressure-volume loops. The Journal of Thoracic and Cardiovascular Surgery. 2006;132(3):610-20. doi: 10.1016/j.jtcvs.2005.12.016.

16.	Zhang S, Uecker M, Voit D, Merboldt KD, Frahm J. Real-time cardiovascular magnetic resonance at high temporal resolution: radial FLASH with nonlinear inverse reconstruction. J Cardiovasc Magn Reson. 2010;12:39. Epub 2010/07/10. doi: 10.1186/1532-429X-12-39. PubMed PMID: 20615228; PubMed Central PMCID: PMCPMC2911425.

17.	Witschey WR, Contijoch F, McGarvey JR, Ferrari VA, Hansen MS, Lee ME, et al. Real-time magnetic resonance imaging technique for determining left ventricle pressure-volume loops. Ann Thorac Surg. 2014;97(5):1597-603. doi: 10.1016/j.athoracsur.2014.01.010. PubMed PMID: 24629301.

18.	Contijoch F, Witschey WR, Rogers K, Rears H, Hansen M, Yushkevich P, et al. User-initialized active contour segmentation and golden-angle real-time cardiovascular magnetic resonance enable accurate assessment of LV function in patients with sinus rhythm and arrhythmias. J Cardiovasc Magn Reson. 2015;17:37. doi: 10.1186/s12968-015-0146-9. PubMed PMID: 25994390; PubMed Central PMCID: PMCPMC4440288.

19.	Dice LR. Measures of the Amount of Ecologic Association Between Species. Ecology. 1945;26(3):297-302.

20.	Bashir MR, Bhatti L, Marin D, Nelson RC. Emerging applications for ferumoxytol as a contrast agent in MRI. Journal of Magnetic Resonance Imaging. 2014;41(4):884-98. doi: 10.1002/jmri.24691.

21.	Turk G, O'Brien JF. Shape transformation using variational implicit functions. Proceedings of the 26th annual conference on Computer graphics and interactive techniques - SIGGRAPH '99: ACM Press; 1999.

22.	Chen Y, Navarro L, Wang Y, Courbebaisse G. Segmentation of the thrombus of giant intracranial aneurysms from CT angiography scans with lattice Boltzmann method. Medical Image Analysis. 2014;18(1):1-8. doi: 10.1016/j.media.2013.08.003.

23.	Wang Y, Navarro L, Zhang Y, Kao E, Zhu Y, Courbebaisse G. Intracranial Aneurysm Phantom Segmentation Using a 4D Lattice Boltzmann Method. Computing in Science & Engineering. 2017;19(4):56-67. doi: 10.1109/mcse.2017.3151252.

24

24.   Wang Y, Zhang Y, Navarro L, Eker OF, Corredor Jerez RA, Chen Y, et al. Multilevel segmentation of intracranial aneurysms in CT angiography images. Medical Physics. 2016;43(4):1777-86. doi: 10.1118/1.4943375.

25.   Kono A, Maughan W, Sunagawa K, Hamilton K, Sagawa K, Weisfeldt M. The use of left ventricular end-ejection pressure and peak pressure in the estimation of the end-systolic pressure-volume relationship. Circulation. 1984;65:988-97.

26.   Tyson GS, Maier GW, Olsen CO, Davis JW, Rankin JS. Pericardial influences on ventricular filling in the conscious dog. An analysis based on pericardial pressure. Circulation Research. 1984;54(2):173-84. doi: 10.1161/01.res.54.2.173.

27.   Kleinbaum DG. Applied regression analysis and other multivariable methods. 4 ed. Belmont: Thomson Brooks/Cole Publishing; 2008.

28.   Olsen CO, Rankin JS, Arentzen CE, Ring WS, McHale PA, Anderson RW. The deformational characteristics of the left ventricle in the conscious dog. Circulation Research. 1981;49(4):843-55. doi: 10.1161/01.res.49.4.843.

29.   Leung JM, Levine EH. Left ventricular end-systolic cavity obliteration as an estimate of intraoperative hypovolemia. Anesthesiology. 1994;81(5):1102-9. Epub 1994/11/01. PubMed PMID: 7978468.

30.   Olsen CO, Tyson GS, Maier GW, Spratt JA, Davis JW, Rankin JS. Dynamic ventricular interaction in the conscious dog. Circ Res. 1983;52(1):85-104. Epub 1983/01/01. PubMed PMID: 6848213.

31.   Contijoch FJ, Witschey WRT, McGarvey J, Lee ME, Gorman J, 3rd, Gorman RC, et al. Slice-by-Slice Pressure-Volume Loop Analysis Demonstrates Native Differences in Regional Cardiac Contractility and Response to Inotropic Agents. Ann Thorac Surg. 2016;102(3):796-802. doi: 10.1016/j.athoracsur.2016.02.055. PubMed PMID: 27112654; PubMed Central PMCID: PMCPMC4995135.

32.   Sun K, Stander N, Jhun CS, Zhang Z, Suzuki T, Wang GY, et al. A computationally efficient formal optimization of regional myocardial contractility in a sheep with left ventricular aneurysm. J Biomech Eng. 2009;131(11):111001. Epub 2009/12/18. doi: 10.1115/1.3148464. PubMed PMID: 20016753; PubMed Central PMCID: PMC2793686.

33.   van der Velde ET, Burkhoff D, Steendijk P, Karsdon J, Sagawa K, Baan J. Nonlinearity and load sensitivity of end-systolic pressure-volume relation of canine left ventricle in vivo. Circulation. 1991;83(1):315-27. PubMed PMID: 1670628.
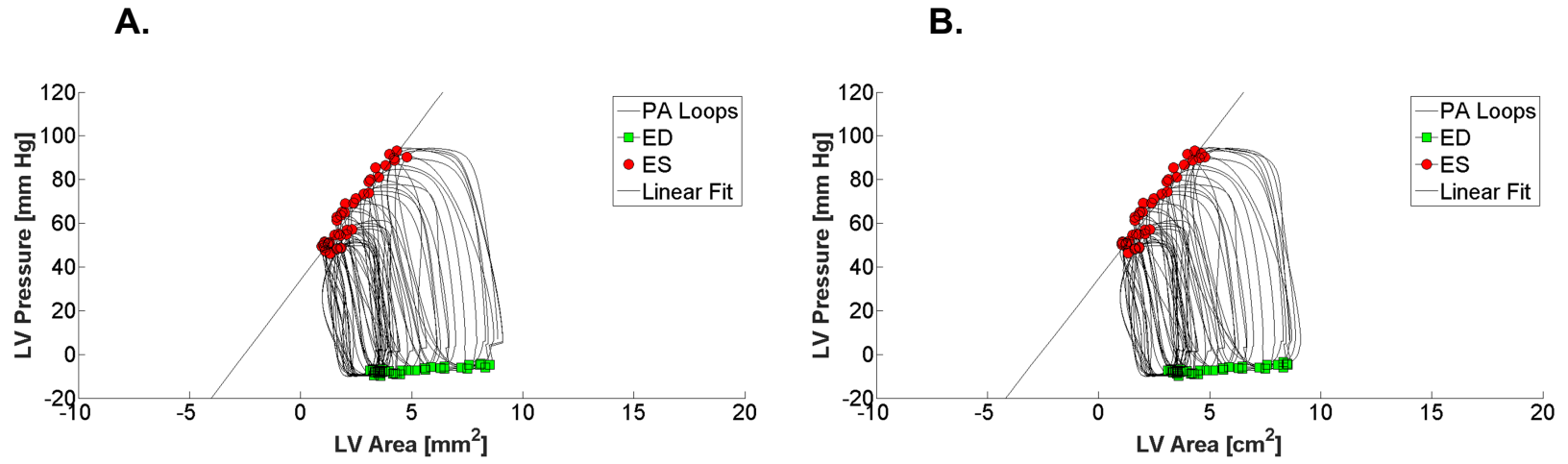
25

S1 Figure.

S1 Figure: Alignment using max + dLVP/dt and max LV area was initially chosen because of the perception that beat shape was more appropriate. In retrospect, there is little effect between this (A) and 0.25 max + dLVP/dt and max LV area (B).

Supporting Information

S1 Figure: Alignment using max + dLVP/dt and max LV area was initially chosen because of the perception that beat shape was more appropriate. In retrospect, there is little effect between this (A) and 0.25 max + dLVP/dt and max LV area (B).

S1 Table: Slope and volume intercept of ESPAR at three LV levels derived from RTMRI-based analysis.

S2 Table: End-systolic elastance E_{ES} (slope) and volume-axis intercept (V_o) estimated from the ESPVR indexed to basal surface volume $(BSA)^{1.5}$.

Figure 1.
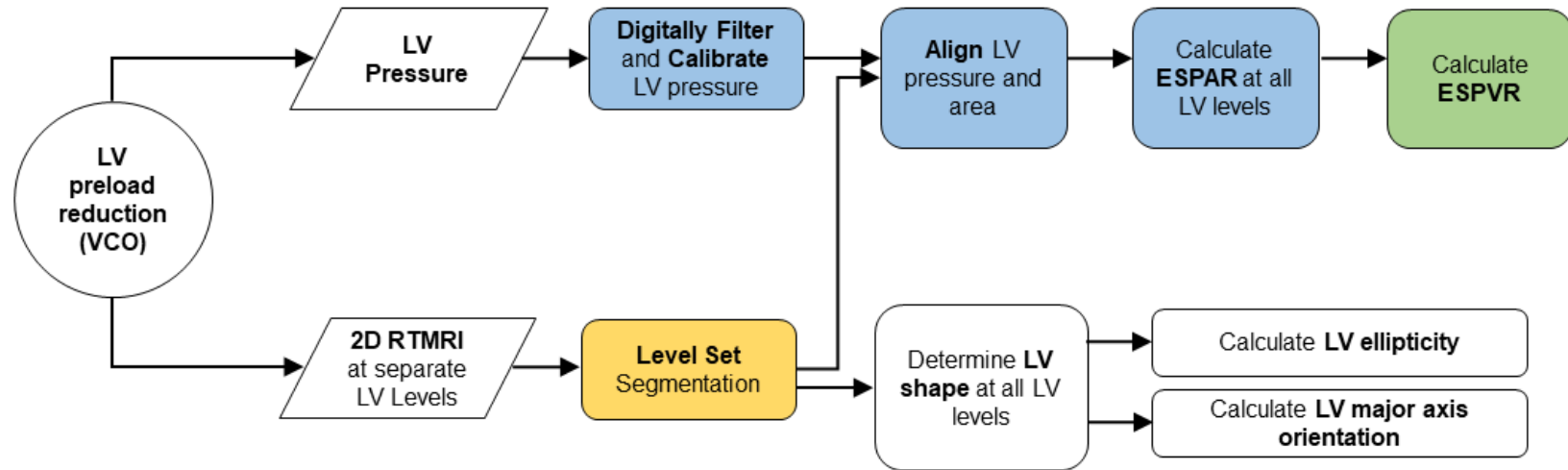
Figure 1: A flowchart illustrating the overall methodology designed to derive subject-specific ESPVR from RTMRI and LV pressure measurement.

☐ - semi-automatic level set segmentation (LSSM) software module

☐ - synchronized pressure area loop generation software module

☐ - ESPVR calculation software module

Figure 2.
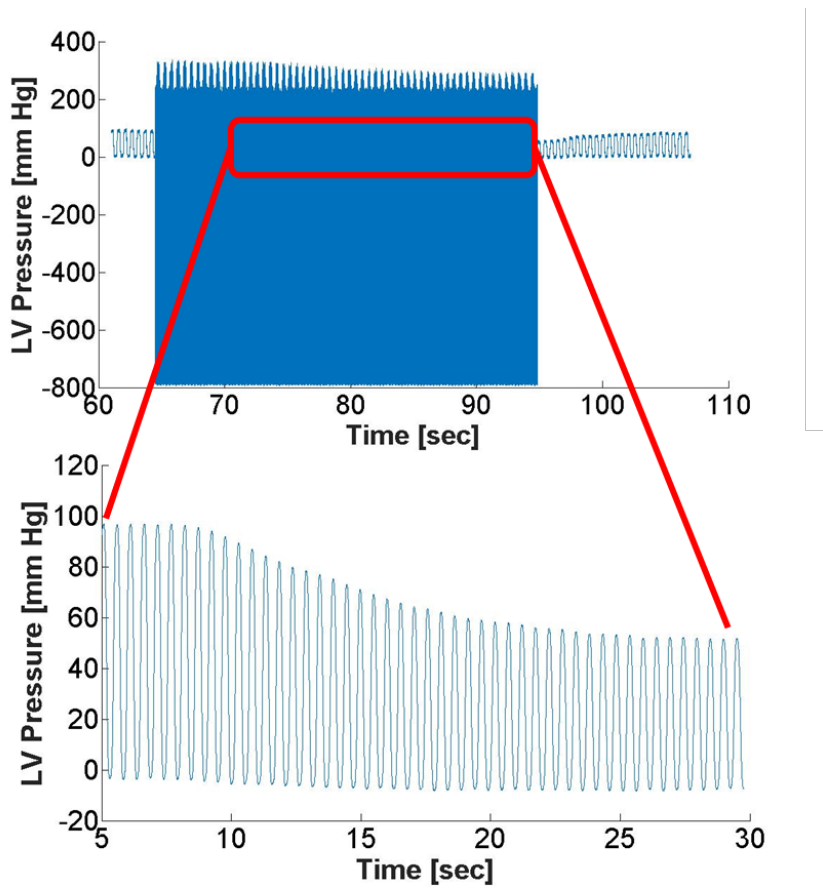
Figure 2: Raw pressure data with noise prior to digital filtering and calibration (top) with the insert showing filtered and calibrated LV pressure during the selected VCO range.

Figure 3.
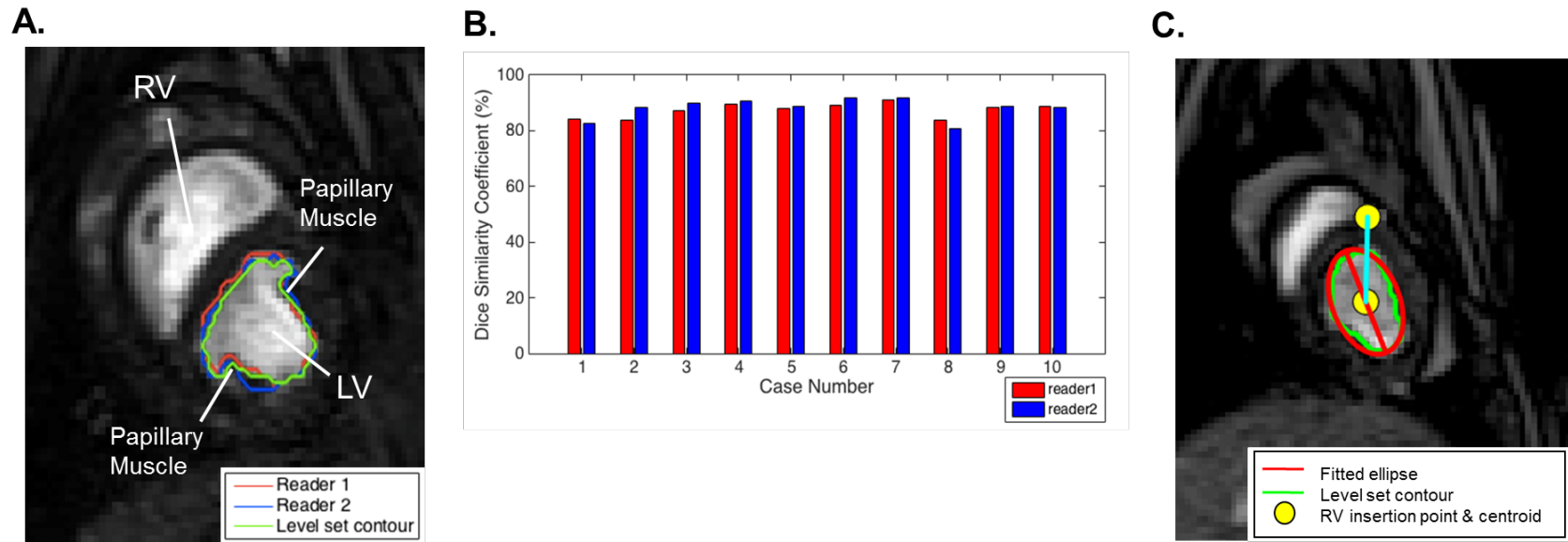
Figure 3: **(A)** Representative midventricular short-axis image of the LV showing level set and manual contours. Green = automatic contouring, Red = manual contour reader 1, Blue = manual contour reader 2. **(B)** Dice similarity coefficient for all 10 cases. **(C)** Representative midventricular short-axis image of the LV overlaid with automatic contours and fitted ellipse for quantifying major/minor axis length and major axis orientation angle as surrogate measurement of LV shape change. Red = fitted ellipse. Green = automatic contouring. Yellow circle = RV insertion point and centroid of ellipse. Movie is included in the Supplementary Material.

Figure 4.
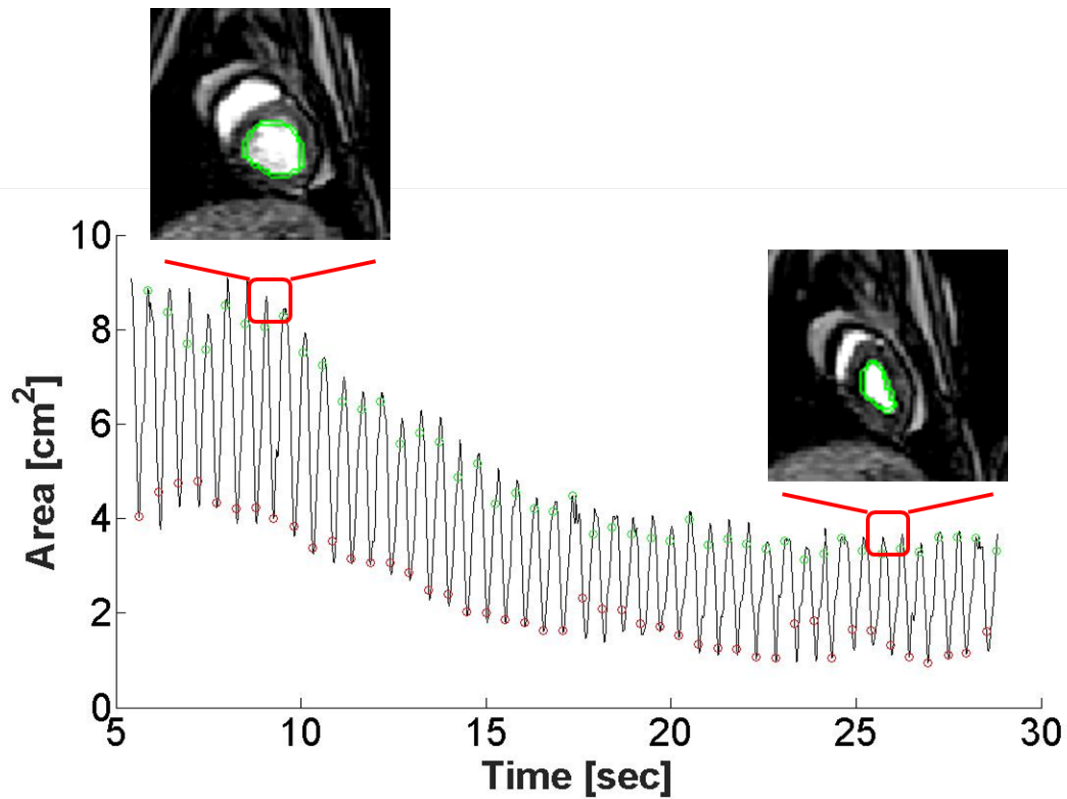
Figure 4: LV Area plot calculated by the level set algorithm with representative midventricular short-axis images of the LV before VCO and during VCO starting at t = 10 sec. Green makers = end-diastole (ED), Red markers = end-systole (ES).
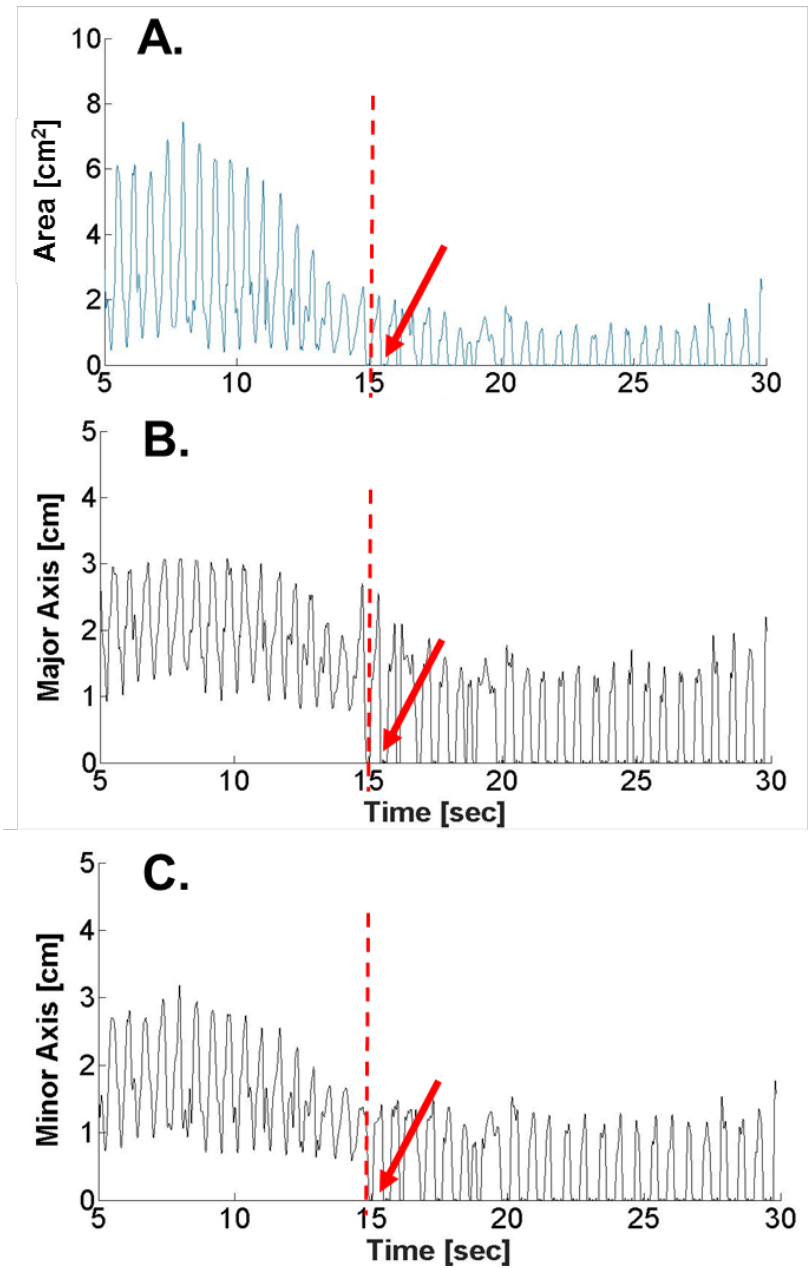
Figure 5.
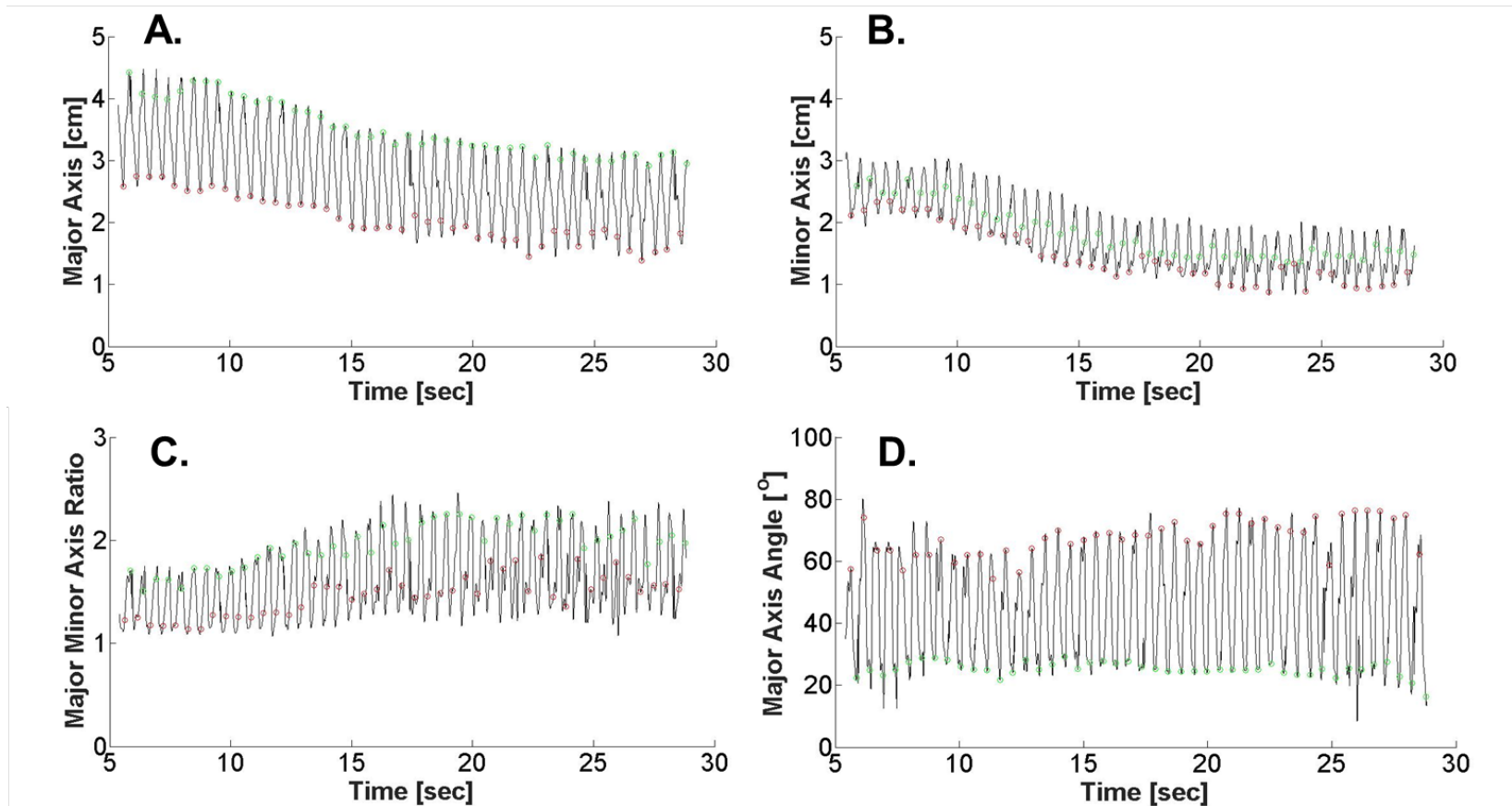
Figure 5: Changes in LV geometry before and during VCO. Shape changes were quantified by 4 indicators calculated from the fitted ellipse:**(A)** Major Axis length, **(B)** Minor Axis length, **(C)** Major to Minor Axis Ratio (MajMinR), and **(D)** Major Axis Orientation Angle. Green makers = end-diastole (ED), Red markers = end-systole (ES).
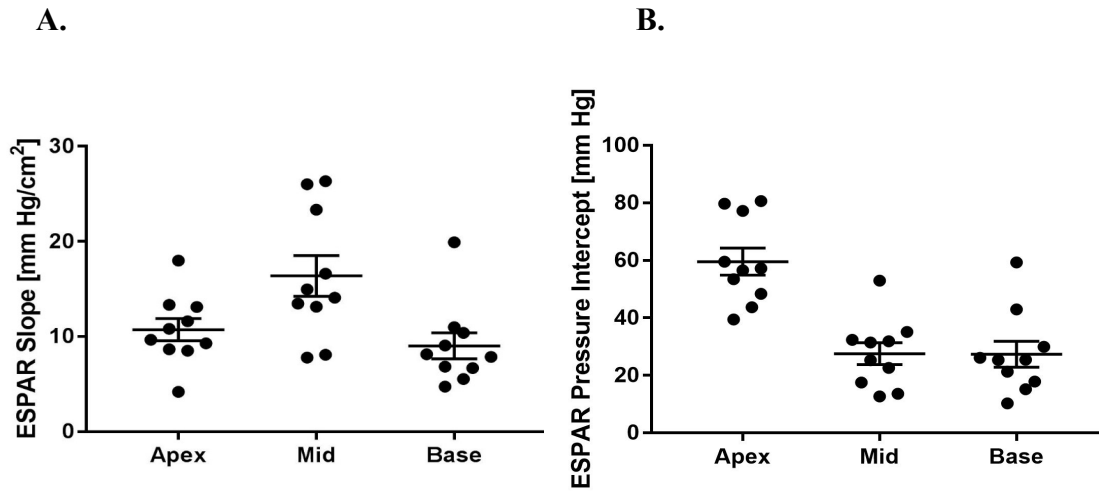
Figure 6.

Figure 6: Plots of LV Apical Area **(A)**, Major Axis length **(B)**, and Minor Axis length **(C)** of a case showing segmental collapse where LVA < 0.25 cm^2 after time $= 15$ sec as indicated by a red arrow. The vertical dashed line represents collapse of the LV to zero volume.

Figure 7.
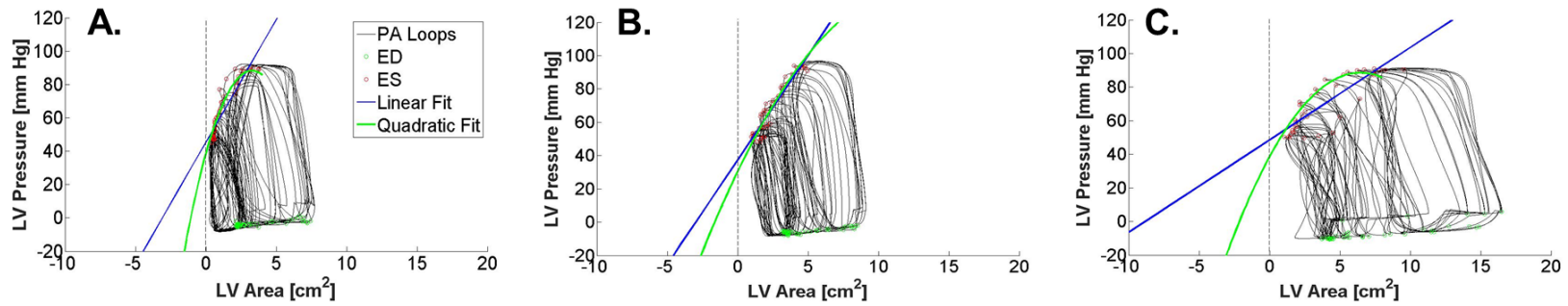
Figure 7: Representative LVP-area (LVPA) loops derived from the level set algorithm and pressure measurements along with fitted ESPAR at apex **(A)**, mid-ventricle **(B)**, and base **(C)** during VCO. The ESPAR was fitted with a linear function (blue) and a quadratic function (green) for comparison. The vertical dashed line represents collapse of the LV to zero volume.
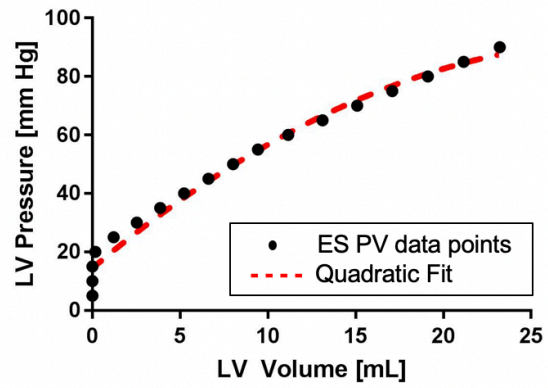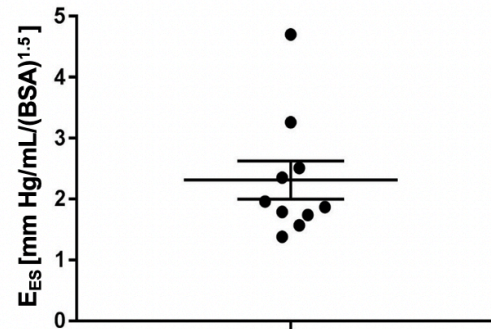
Figure 8.

A.　　　　　　　　　　　　　　　　**B.**

Figure 8: Slope of ESPAR **(A)** and LV area intercept A_o **(B)** at apex, mid, and base LV levels for all animals indexed to basal surface volume.
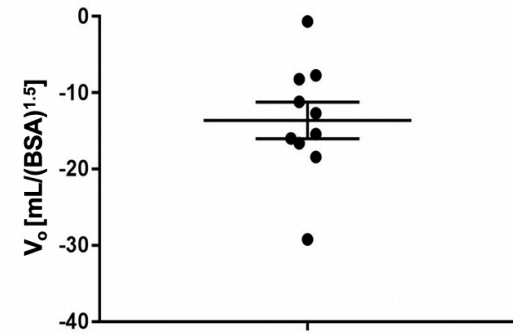
Figure 9.

Fig 9: Representative ESPVR with a quadratic fit in red dashed line **(A).** End-systolic elastance E_{ES} **(B)** and volume intercept V_o **(C)** of ESPVR indexed to basal surface volume.